

Detection of slow slip events using wavelet analysis of GNSS recordings

Ariane Ducellier¹, Kenneth C. Creager¹, and David A. Schmidt¹

¹University of Washington, Department of Earth and Space Sciences, Box 351310, 4000 15th Avenue NE Seattle, WA 98195-1310

Key points

- 8 • We use a wavelet-based signal processing method to detect slow slip events
9 in GNSS data.

10 • There is a good correlation between events detected with GNSS data and
11 events detected with seismic data.

12 • The method could be applied in regions and no tremor are detected in
13 conjunction with slow slip events.

14 **Abstract**

15 Slow slip events were discovered in many subduction zones during the last two
16 decades thanks to recordings of the displacement of Earth's surface by GNSS
17 networks. Slow slip can last from a few days to several years and has a rel-
18 atively short recurrence time (months to years), compared to the recurrence
19 time of regular earthquakes (up to several hundreds of years). In many places,
20 tectonic tremor is also observed in relation to slow slip and can be used as a
21 proxy to study slow slip events of moderate magnitude where surface defor-
22 mation is hidden in GNSS noise. However, in subduction zones where no clear
23 relationship between tremor and slow slip occurrence is observed, these methods
24 cannot be applied, and we need other methods to be able to better detect and
25 quantify slow slip. In this paper, we use the Maximal Overlap Discrete Wavelet
26 Transform (MODWT) to analyze GNSS time series and seismic recordings of
27 slow slip events in Cascadia. We use detrended GNSS data, apply the MODWT
28 transform and stack the wavelet details over several nearby GNSS stations. As
29 an independent check on the timing of slow slip events, we also compute the
30 cumulative number of tremor in the vicinity of the GNSS stations, detrend this
31 signal, and apply the MODWT transform. In both time series, we can then
32 see simultaneous waveforms whose timing corresponds to the timing of slow slip
33 events. We assume that there is a slow slip event whenever there is a peak in
34 the wavelet signal. We verify that there is a good correlation between slow slip
35 events detected with only GNSS data, and slow slip events detected with only
36 seismic data. The wavelet-based detection method detects all events of magni-
37 tude higher than 6 as determined by independent event catalogs (e.g. Michel
38 et al. [2019]).

39 **1 Introduction**

40 Slow slip events are a new feature discovered in the last two decades in many
41 subduction zones thanks to recordings of the displacement of Earth's surface by
42 dense Global Navigation Satellite System (GNSS) networks. As with ordinary
43 earthquakes, slow slip events are caused by slip on a fault, such as the plate
44 boundary between a tectonic plate subducting under another tectonic plate.
45 However, they take a much longer time (several days to several years) to hap-
46 pen relative to ordinary earthquakes, and they have a relatively short recurrence
47 time (months to years), compared to the recurrence time of regular earthquakes
48 (up to several hundreds of years), allowing scientists to observe and study many
49 complete event cycles, which is typically not possible to explore with traditional
50 earthquake catalogs [Beroza and Ide, 2011]. A slow slip event on the plate
51 boundary is inferred to happen when there is a reversal of the direction of mo-
52 tion at GNSS stations, compared to the secular interseismic motion. Slow slip
53 events have been observed in many subduction zones, such as Cascadia, Nankai
54 (southwest Japan), Alaska, Costa Rica, Mexico, and New Zealand [Beroza and
55 Ide, 2011, Audet and Kim, 2016].

56 In many places, tectonic tremor are also observed in relation to slow slip.
57 Tremor is a long (several seconds to many minutes), low amplitude seismic signal,
58 with emergent onsets, and an absence of clear impulsive phases. Tectonic
59 tremor have been explained as a swarm of small, low-frequency earthquakes
60 (LFEs) [Shelly et al., 2007], that is small magnitude earthquakes ($M \sim 1$),
61 for which frequency content (1-10 Hz) is lower than for ordinary earthquakes
62 (up to 20 Hz). In subduction zones such as Nankai and Cascadia, tectonic
63 tremor observations are spatially and temporally correlated with slow slip ob-
64 servations [Obara, 2002, Rogers and Dragert, 2003]. Due to this correlation,
65 these paired phenomena have been called Episodic Tremor and Slip (ETS).
66 However, this is not always the case. For instance, in northern New Zealand,
67 tremor are more challenging to detect, and seem to be located downdip of the
68 slow slip on the plate boundary.

70 In Cascadia and Guerrero, Mexico, tremor has been used as a proxy to ob-
71 serve slow slip events that are not directly detectable in the GNSS data. For
72 instance, Aguiar et al. [2009] studied 23 ETS events in Cascadia with more
73 than 50 hours of tectonic tremor. For all these events, they computed both
74 the GPS-estimated moment release and the cumulative number of hours of tec-
75 tonic tremor recorded. They observed a linear relationship between moment
76 release and number of hours of tremor for ETS events of moment magnitude
77 6.3 to 6.8. They also observed many smaller bursts of tremor of duration 1 to
78 50 hours in between the big ETS events, without any detectable signal in the
79 GPS data. However, based on the relationship between slow slip moment and
80 number of hours of tremor for bigger events, it is possible to infer the existence
81 of smaller slow slip events of magnitude 5-6 occurring simultaneously with the
82 tremor bursts.

84 Frank [2016] divided GPS time series observations into two groups: the
85 first group contains days when slow seismicity (tectonic tremor and LFEs) is
86 detected, the second group contains days when the numbers of tremor or LFEs
87 is lower than a threshold. He then stacked separately the two groups of obser-
88 vations and observed a cumulative displacement in the northern direction (for
89 Guerrero) and the eastern direction (for Cascadia) corresponding to the load-
90 ing period when few tremor or LFEs are observed and the surface deformation
91 corresponds to the secular plate motion. He also observed a cumulative dis-
92 placement in the southern direction (for Guerrero) and the western direction
93 (for Cascadia) corresponding to the release period when tremor and LFEs are
94 observed. He was thus able to observe a reverse displacement corresponding to
95 smaller slow slip events not directly observable in the GPS data.

97 However, in other subduction zones such as New Zealand, there is no clear
98 relationship between tremor and slow slip occurrence and these methods cannot
99 be applied to detect smaller slow slip events that produce a GNSS signal with
100 an amplitude too small compared to the noise. We thus need other methods to

102 be able to better detect and quantify slow slip.

103
104 Wavelets methods such as the Discrete Wavelet Transform (DWT) are mathematical tools for analyzing time series simultaneously in the time and the frequency domain by observing how weighted averages of a time series vary from one averaging period to the next. Wavelet methods have been widely used for geophysical applications [Kumar and Foufoula-Georgiou, 1997]. However, few studies have used wavelet methods to analyze recordings of slow slip, and their scope was limited to the detection of the bigger (magnitude 6-7) short-term (a few weeks) events [Szeliga et al., 2008, Ohtani et al., 2010, Wei et al., 2012, Alba et al., 2019].

113
114 Szeliga et al. [2008] determined the timing and the amplitude of 34 slow slip events throughout the Cascadia subduction zone between 1997 and 2005. They modeled the GPS time series by the sum of a linear trend, annual and biannual sinusoids representing seasonal effects, Heaviside step functions corresponding to earthquakes and hardware upgrades, and a residual signal. They then applied a Gaussian wavelet transform to the residual time series to get the exact timing of the slow slip at each GPS station. The idea is that the wavelet transform allows us to analyze the signal both in the time and the frequency domains. A sharp change in the signal will be localized and seen at all levels of the wavelet decomposition, contrary to what happens with the periodic sinusoids of the Fourier transform.

125
126 Instead of using wavelets in the time domain, Ohtani et al. [2010] used 2D wavelet functions in the spatial domain to detect slow slip events. They designed the Network Stain Filter (NSF) to detect transient deformation signals from large-scale geodetic arrays. They modeled the position of the GPS station by the sum of the secular velocity, a spatially coherent field, site-specific noise, reference frame errors, and observation errors. The spatial displacement field is modeled by the sum of basis wavelets with time-varying weights. Their method has been successfully used to detect a transient event in the Boso peninsula, Japan, and a slow slip event in the Alaska subduction zone [Wei et al., 2012].

135
136 Finally, Alba et al. [2019] used hourly water level records from four tide gauges in the Juan de Fuca Straight and the Puget Sound to determine vertical displacements, uplift rates between ETS events, and net uplift rates between 1996 and 2011. Their main idea is that the tidal level measured at a given gauge is the sum of a noise component at multiple timescales (tides, ocean and atmospheric noise) and an uplift signal due to the ETS events. The noise component is assumed to be coherent between all tidal gauges, while the uplift signal is different provided that the gauges are far enough from each other. By stacking the tidal records, the uplift signals cancel each other while the noise signal is amplified. By stacking the details of the DWT decomposition, instead of stacking the raw tidal record, each of the components of the noise at different time scales is retrieved and can then be removed from the raw records to obtain

148 the uplift signal. The authors were then able to clearly see a difference in uplift
149 between the two tidal gauges at Port Angeles and Port Townsend.

150

151 In our study, we use a similar approach with a different reasoning. We only
152 stack signals at nearby GPS stations, assuming that the longitudinal displace-
153 ment due to the ETS events will then be the same at each of the GPS stations
154 considered. We suppose that some of the noise component is different at each
155 GPS station and will be eliminated by the stacking. Finally, we suppose that
156 the noise and the longitudinal displacement due to the ETS events and the sec-
157 ular plate motion have different time scales, so that the wavelet decomposition
158 will act as a bandpass filter to retrieve the displacement signal and highlight the
159 ETS events. We use wavelet methods to analyze GPS and seismic recordings
160 of slow slip events in Cascadia. Our objective is to verify that there is a good
161 correlation between slow slip events detected with only GNSS data, and slow
162 slip events detected with only seismic data. We thus want to demonstrate that
163 the wavelet-based detection method can be applied to detect slow slip events
164 that may be currently undetected with standard methods.

165

166 2 Data

167 We focused our study on northwest Washington State. For the GNSS data, we
168 used the GPS time series provided by the Pacific Northwest Geodetic Array,
169 Central Washington University. These are network solutions in ITRF2008 with
170 phase ambiguities resolved. Solutions are computed with JPL/NASA orbits and
171 satellite clocks. North, East, and Vertical directions are available. However, as
172 the direction of the secular plate motion is close to the East direction, we only
173 used the East direction of the GPS time series for the data analysis, as it has
174 the best signal-to-noise ratio. The wavelet method works best with data with
175 zero mean, and no sharp discontinuities, so we use the cleaned dataset, that is
176 GPS times series with linear trends, steps due to earthquakes or hardware up-
177 grades, and annual and semi-annual sinusoids signals simultaneously estimated
178 and removed following Szeliga et al. [2004]. For the seismic data, we used the
179 tremor catalog from [reference for the catalog](#). The following is to be modified.
180 [the Pacific Northwest Seismic Network \(PNSN\)](#) [Wech, 2010]. Tremor were
181 detected and located using waveform envelope correlation and clustering and
182 a centroid location is available for every given five-minute time window when
183 tremor was detected. As the catalog starts in August 2009, we only looked at
184 GPS data recorded in 2009 or later.

185

186 **3 Method**

187 **3.1 The Maximal Overlap Discrete Wavelet Transform**

188 The Discrete Wavelet Transform (DWT) is an orthonormal transform that
 189 transforms a time series X_t ($t = 0, \dots, N - 1$) into a vector of wavelet coeffi-
 190 cients W_i ($i = 0, \dots, N - 1$). If we denote J the level of the wavelet decom-
 191 position, and we have $N = n * 2^J$, where n is some integer higher or equal to 1,
 192 the vector of wavelet coefficients can be decomposed into J wavelet vectors W_j
 193 of lengths $\frac{N}{2}, \frac{N}{4}, \dots, \frac{N}{2^J}$, and one scaling vector V_J of length $\frac{N}{2^J}$. Each wavelet
 194 vector W_j is associated with changes on scale $\tau_j = dt2^{j-1}$, where dt is the time
 195 step of the time series, and corresponds to the filtering of the original time series
 196 with a filter with nominal frequency interval $[\frac{1}{dt2^{j+1}}; \frac{1}{dt2^j}]$. The scaling vector
 197 V_J is associated with averages in scale $\lambda_J = dt2^J$, and corresponds to the fil-
 198 tering of the original time series with a filter with nominal frequency interval
 199 $[0; \frac{1}{dt2^{j+1}}]$. We can also define for $j = 1, \dots, J$ the j th wavelet detail D_j , which
 200 is a vector of length N , and is associated to scale $\tau_j = dt2^{j-1}$. Similarly, we can
 201 define for $j = 1, \dots, J$ the j th wavelet smooth S_j , which is a vector of length
 202 N , and is associated to scales $\tau_{j+1} = dt2^{j+1}$ and higher. Together, the details
 203 and the smooths define the multiresolution analysis (MRA) of X :

204

$$X = \sum_{j=1}^J D_j + S_J \quad (1)$$

205 The DWT present several disadvantages. First, the length of the time se-
 206 ries must be a multiple of 2^J where J is the level of the DWT decompositon.
 207 Second, the time step of the wavelet vector W_j is $dt2^j$, which may not corre-
 208 spond to the time when some interesting phenomenon is visible on the original
 209 time series. Third, when we circularly shift the time series, the corresponding
 210 wavelet coefficients, details and smooths are not a circularly shifted version of
 211 the wavelet coefficients, details and smooths of the original time series. Thus,
 212 the values of the wavelet coefficients, details and smooths are strongly depen-
 213 dent on the time when we start experimentally gathering the data. Finally,
 214 when we filter the time series to obtain the details and smooths, we introduce
 215 a phase shift, which makes difficult to line up meaningfully the features of the
 216 MRA with the original time series.

217 This is why we use instead the Maximal Overlap Discrete Wavelet Transform
 218 (MODWT). The MODWT transforms the time series X_t ($t = 0, \dots, N - 1$) into J
 219 wavelet vectors \tilde{W}_j ($j = 1, \dots, J$) of length N and a scaling vector \tilde{V}_J of length
 220 N . As is the case for the DWT, each wavelet vector \tilde{W}_j is associated with
 221 changes on scale $\tau_j = dt2^{j-1}$, and corresponds to the filtering of the original time
 222 series with a filter with nominal frequency interval $[\frac{1}{dt2^{j+1}}; \frac{1}{dt2^j}]$. The scaling
 223 vector \tilde{V}_J is associated with averages in scale $\lambda_J = dt2^J$, and corresponds to the
 224 filtering of the original time series with a filter with nominal frequency interval
 225 $[0; \frac{1}{dt2^{j+1}}]$. As is the case for the DWT, we can write the MRA:

$$X = \sum_{j=1}^J \tilde{D}_j + \tilde{S}_J \quad (2)$$

The MODWT of a time series can be defined for any length N . The time step of the wavelet vectors \tilde{W}_j and the scaling vector \tilde{V}_J is equal to the time step of the original time series. When we circularly shift the time series, the corresponding wavelet vectors, scaling vector, details and smooths are shifted by the same amount. The details and smooths are associated with a zero phase filter, making it easy to line up meaningfully the features of the MRA with the original time series. The wavelet methods for time series analysis are explained in a more detailed way in [Percival and Walden, 2000]).

236

3.2 Application to synthetic data

To illustrate the wavelet transform method, we first apply the MODWT to synthetics data. As slow slip events occur in Cascadia on a regular basis, every twelve to eighteen months, we create a synthetic signal of period $T = 500$ days. To reproduce the ground displacement observed on the longitudinal component of GPS stations in Cascadia, we divide each period into two parts: In the first part of duration $T - N$, the displacement is linearly increasing and corresponds to the secular plate motion in the eastern direction; in the second part of duration N , the displacement is linearly decreasing and corresponds to a slow slip event on a reverse fault at depth triggering a ground displacement in the western direction. To see the effect of the magnitude of the slow slip event, we use different values for $N = 5, 10, 20, 40$ days. Figure 1 shows the synthetics, the details of the wavelet decomposition for levels 1 to 10, and the smooth for the four durations of a slow slip event.

251

The ramp-like signal is transformed through the wavelet filtering into a waveform with first a positive peak and then a negative peak. The shape of the waveform is the same for every level of the wavelet decomposition, but the width of the waveform increases with the scale level. For the 8th level of the wavelet decomposition, the width of the waveform is nearly as large as the time between two events. At larger scales, the waveforms start to merge two contiguous events together, and make the wavelet decomposition less interpretable. For an event of duration 5 days, the wavelet details at levels higher than 3 have a larger amplitude than the wavelet details at lower scales. For an event of duration 10 days, the wavelet details at levels higher than 4 have a larger amplitude than the wavelet details at lower scales. For an event of duration 20 days, the wavelet details at levels higher than 5 have a larger amplitude than the wavelet details at lower scales. For an event of duration 40 days, the wavelet details at levels higher than 6 have a larger amplitude than the wavelet details at lower scales. Thus, the scale levels at which an event is being seen in the wavelet details give us an indication about the duration (and the magnitude) of the slow slip event.

268 We expect the big slow slip events of magnitude 6-7 that last several weeks to
269 start being visible at the level 5 of the wavelet decomposition, but to not be
270 noticeable at lower time scales.

271

272 3.3 MODWT of GPS and tremor data

273 The DWT and MODWT methods must be used on a continuous time series,
274 without gaps in the recordings. To deal with the gaps in the GNSS record-
275 ings, we simply replace the missing values by the sum of a straight line and a
276 Gaussian noise component with mean zero and standard deviation equal to the
277 standard deviation of the whole time series. The straight line starts at the mean
278 of the five days before the gap and ends at the mean of the five days after the
279 gap. We verify how the wavelet details may be affected by looking at a GPS
280 time series without missing values and comparing the wavelet details with and
281 without removing some data points. Station PGC5 has recorded during 1390
282 days between 2009 and 2013, without any missing values. We first computed
283 the wavelet details without missing values. Then, we removed ten neighboring
284 missing values, replaced them by the sum of the straight line and the Gaussian
285 noise component, and computed the wavelet details with the replaced values.
286 Figure 2 shows a comparison of the two wavelet details for two different loca-
287 tions of the missing values. We can see that there are visible differences in the
288 time series itself, and in the details at the smallest levels of the wavelet decom-
289 position. However, the differences between the wavelet details with and without
290 missing values get smaller and smaller with increasing levels the details, and are
291 barely visible for the levels we are mostly interested in (levels 6 and above). We
292 thus conclude that we can easily replace the missing values in the GNSS time
293 series without introducing false detections of slow slip events.

294

295 We then applied the wavelet filtering to real GPS data. Figure 3 shows the
296 longitudinal displacement for GPS station PGC5, located in southern Vancou-
297 ver Island, the details of the wavelet decomposition for levels 1 to 8, and the
298 smooth. In the data, we can see a sharp drop in displacement whenever there
299 is a slow slip event. For levels 5 to 8, we can see in the details a positive peak
300 followed by a negative peak whenever there is a drop in displacement in the
301 data. We thus verify that the wavelet method can detect slow slip events.

302

303 To increase the signal-to-noise ratio and be able to better detect slow slip
304 events, we stack the signal over several GPS stations. We choose to focus on
305 GPS stations located close enough to the tremor zone to get a sufficiently high
306 amplitude of the slow slip signal. We choose 16 points located on the 40 km
307 depth contour of the plate boundary (model from Preston et al. [2003]) with
308 spacing equal 0.1 degree in latitude (red triangles on Figure 4). Then we took
309 all the GPS stations located in a 50 km radius for a given point, compute the
310 wavelet details for the longitudinal displacement of each station, and stack each
311 detail over the GPS stations. We thus have a stacked detail for each level 1 to

312 10 of the wavelet decomposition.

313

314 To compare slow slip events detected with GPS data and slow slip events
315 detected with seismic data, we took all the tremor epicenters located within
316 a 50 km radius centered on one of the 16 locations marked by red triangles
317 on Figure 3. Then we computed the cumulative number of tremor within this
318 circle. Finally, we removed a linear trend from the cumulative tremor count,
319 and applied the wavelet transform. Figure 5 shows an example of the wavelet
320 decomposition for the third northernmost location on Figure 4 (which is closest
321 to GPS station PGC5). Contrary to what happens for the GPS data, we see a
322 sharp increase in the data whenever there is a tremor episode, which translates
323 into a negative peak followed by a positive peak in the wavelet details.

324 4 Results

325 We stacked the 8th level detail of the wavelet decomposition of the displacement
326 over all the GPS stations located in a 50 km radius of a given point, for
327 the 16 locations indicated in Figure 3. The result is shown in the top panel of
328 Figure 6, where each line represents one of the locations. To better highlight
329 the peaks in the wavelet details, we highlighted in red the time intervals where
330 the amplitude of the stacked detail is higher than a threshold, and in blue the
331 time intervals where the amplitude of the stacked detail is lower than minus
332 the threshold. To compare the GPS signal with the tremor signal, we plotted
333 the 8th level detail of the wavelet decomposition of the tremor count on the
334 bottom panel of Figure 6. We used the opposite of the cumulative tremor count
335 for the wavelet decomposition in order to be able to match positive peaks with
336 positive peaks and negative peaks with negative peaks. In the tremor catalog
337 from [reference?](#), there are 17 tremor events with more than 150 hours of tremor
338 recorded. The events are summarized in Table 1. The time of the event is the
339 start date plus half the duration of the event. Although the latitudinal extension
340 of the events is not always the same for the GPS data and for the tremor data,
341 we identify the same 13 events in both 8th wavelet decompositions for the 8th
342 level: January 2007, May 2008, May 2009, August 2010, August 2011, September
343 2012, September 2013, August-November 2014, January 2016, March 2017,
344 June 2018, March-November 2019, and October 2020-January 2021. Although
345 there are two events in the tremor catalog in August 2014 and November 2014,
346 these two events are not distinguishable in the 8th level details and look more
347 like a single event slowly propagating from South to North. The same phe-
348 nomenon is observed in 2019 when two tremor events in March and November
349 2019 are merged into a single event propagating slowly from South to North.
350 In 2020-2021, the wavelet decomposition of the tremor shows one event in the
351 south in October-November 2020 and one event in the North in January 2021,
352 but in the wavelet decomposition of the GPS data, these three events look like
353 a single event propagating slowly from South to North.

354

355 Figures 7 and 8 show the same comparison between the wavelet decomposi-
 356 tion of the GPS data and the wavelet decomposition of the tremor count data
 357 for the 7th level and the 6th level respectively. For the 7th level, we see the
 358 same events as for the 8th level, both for the GPS data and the tremor count
 359 data. The wavelet decomposition is more noisy for the GPS data between 2010
 360 and 2012, but it does not seem that there are more slow slip events visible in
 361 the 7th level.

362

363 For the 6th level detail, we see an additional event in the South in Fall 2009
 364 that is present both in the GPS and the tremor data. It may correspond to the
 365 northern extent of a big ETS event occurring in Fall 2009 south of the study
 366 area (event 19 in the Michel et al. [2019] catalog). There are three small signals
 367 in the GPS data in Spring 2012, Fall 2017, and Winter 2020 that are not present
 368 in the tremor data, and are probably false detections. To summarize, all the 13
 369 events present on the 7th and 8th level details of the wavelet decomposition are
 370 true detections, 14 of the 17 events present on the 6th level detail of the wavelet
 371 decomposition are true detections.
 372

373 5 Discussion

374 To better evaluate the number of true and false detections, we convert the
 375 wavelet details into binary time series. If the absolute value of the wavelet
 376 detail is higher than a threshold, we replace the value by 1 (for positive values)
 377 or -1 (for negative values), otherwise we replace the value by 0. We do this
 378 on both the wavelet details of the GPS data and of the tremor data. Then we
 379 decide that if both the GPS and the tremor time series take the value 1 (or
 380 both take the value -1), we have a true detection (true positive TP). If the GPS
 381 and the tremor time series have opposite signs, or if the absolute value of the
 382 GPS time series is 1 but the value of the tremor time series is 0, we have a
 383 false detection (false positive FP). If both time series take the value 0, we do
 384 not have detection (true negative TN). If the GPS time series take the value 0,
 385 but the absolute value of the tremor time series is 1, we miss a detection (false
 386 negative). We then define the sensitivity (true positive rate) and the specificity
 387 (equal to 1 minus the false positive rate) as:

$$\begin{aligned}
 \text{sensitivity} &= \frac{TP}{TP + FN} \\
 \text{specificity} &= \frac{TN}{TN + FP}
 \end{aligned} \tag{3}$$

388 We can then evaluate the quality of the detections obtained with our method
 389 by plotting a receiver operating characteristic curve (ROC curve). The ROC
 390 curve is widely used for binary classification problems, and is plotted by varying
 391 the values of the threshold (here the thresholds used to convert the GPS and
 392 the tremor time series into binary time series), computing the corresponding

393 values of the true positive rate and the false positive rate (equal to 1 minus the
394 specificity), and plotting the true positive rate as a function of the false positive
395 rate. If the classification was made randomly, all the points would fall on the
396 first diagonal. If the classifier was perfect, the corresponding point would fall
397 on the top left corner of the graph with true positive rate equal to 1 and false
398 positive rate equal to 0. The bigger the area under the curve, the better the
399 classifier is.

400

401 As the slow slip events are better seen on levels 6, 7 and 8 of the wavelet
402 decomposition, we first add the wavelet details corresponding to levels 6 to 8,
403 and transform the resulting time series into a binary time series. We apply
404 this transform to both the GPS and the tremor time series with varying thresh-
405 olds. We then plot the ROC curve on Figure 8. The corresponding sums of
406 the wavelet details for the GPS data and the tremor data are shown on Figure
407 10. We can see that there is a trade-off between sensitivity and specificity. If
408 we decrease the false positive rate, we also decrease the number of true events
409 detected. If we increase the number of true events detected, we also increase
410 the false positive rate.

411

412 In addition to the magnitude 6 events discussed above, Michel et al. [2019]
413 have also identified several magnitude 5 events using a variational Bayesian In-
414 dependent Component Analysis (vbICA) decomposition of the signal. As we
415 expect smaller magnitude events to be more visible at smaller time scales of
416 the wavelet decomposition (level 5), we verify for all these events whether a
417 signal can be seen at the same time as the time given in their catalog. Most
418 of these magnitude 5 events are also sub-events of bigger magnitude 6 events.
419 Table 2 summarizes for each event its timing, its number and its magnitude as
420 indicated in the catalog from Michel et al. [2019], and whether it is part of a
421 bigger magnitude 6 event.

422

423 Figure 11 shows the 5th level detail wavelet decomposition of the GPS data.
424 Red lines show the timing of the big ETS events from Table 1, and blue lines
425 show the timing of the small slow slip events from Table 2.

426

427 All 14 events that are sub-event of a bigger event are visible at level 5.
428 However, this may be due because the bigger event are clearly seen at levels 6
429 to 8, and also at smaller time scales. The one small event that is not part of
430 a bigger event (Winter 2009) is visible at level 5 of the wavelet decomposition.
431 However, some other events that are not in Michel et al. [2019]’s catalog are
432 also visible in late 2007, early 2010, early 2012, and late 2016. Therefore, it is
433 difficult to make the difference between a true detection and a false detection,
and to conclude whether the method can indeed detect events of magnitude 5.

434 **6 Conclusion**

435 In this paper, we have used wavelet methods to analyze GNSS time series and
436 seismic recordings of slow slip events in Cascadia. We used detrended GNSS
437 data, applied the MODWT transform and stack the wavelet details over several
438 nearby GNSS stations. As an independent check on the timing of slow slip
439 events, we also computed the cumulative number of tremor in the vicinity of
440 the GNSS stations, detrended this signal, and applied the MODWT transform.
441 In both time series, we could then see simultaneous waveforms whose timing
442 corresponds to the timing of slow slip events. We assumed that there is a slow
443 slip event whenever there is a peak in the wavelet signal. We verified that
444 there is a good correlation between slow slip events detected with only GNSS
445 data, and slow slip events detected with only seismic data. The wavelet-based
446 detection method detects all events of magnitude higher than 6 as determined
447 by independent event catalogs (e.g. [Michel et al., 2019]). We detected signals
448 in the GPS data that could be magnitude 5 events, but it is not easy to make
449 the difference between true detections and false detections.

450 **Data and Resources**

451 The GPS recordings used for this analysis can be downloaded from the PANGA
452 website [GPS/GNSS Network and Geodesy Laboratory: Central Washington
453 University, other/seismic network, 1996] <http://www.panga.cwu.edu/>. Reference
454 for tremor catalog. The Python scripts used to analyze the data and
455 make the figures can be found on the first author's Github account <https://github.com/ArianeDucellier/slowslip>. Figure 4 was done using GMT
456 [Wessel and Smith, 1991].
457

458 **Acknowledgements**

459 This work was funded by the grant from the National Science Foundation XXX.
460 A.D. would like to thank Pr Donald Percival for introducing her to wavelet
461 methods during his excellent class taught at University of Washington.

462 **Declaration of Competing Interests**

463 The authors declare no competing interests.

464 **References**

465 A.C. Aguiar, T.I. Melbourne, and C.W. Scrivner. Moment release rate of Cas-
466 cadia tremor constrained by GPS. *Journal of Geophysical Research*, 114:
467 B00A05, 2009.

- 468 S. Alba, R. J. Weldon, D. Livelybrooks, and D. A. Schmidt. Cascadia ETS
469 events seen in tidal records (1980–2011). *Bulletin of the Seismological Society*
470 *of America*, 2019.
- 471 P. Audet and Y.H. Kim. Teleseismic constraints on the geological environment
472 of deep episodic slow earthquakes in subduction zone forearcs: A review.
473 *Tectonophysics*, 670:1–15, 2016.
- 474 G.C. Beroza and S. Ide. Slow earthquakes and nonvolcanic tremor. *Annual*
475 *Review of Earth and Planetary Sciences*, 39:271–296, 2011.
- 476 W.B. Frank. Slow slip hidden in the noise: The intermittence of tectonic release.
477 *Geophysical Research Letters*, 43:10125–10133, 2016.
- 478 GPS/GNSS Network and Geodesy Laboratory: Central Washington University,
479 other/seismic network. Pacific Northwest Geodetic Array (PANGA), 1996.
480 URL <http://www.panga.cwu.edu/>.
- 481 P. Kumar and E. Foufoula-Georgiou. Wavelet analysis for geophysical applica-
482 tions. *Reviews of Geophysics*, 35(4):385–412, 1997.
- 483 S. Michel, A. Gualandi, and J.-P. Avouac. Interseismic coupling and slow slip
484 events on the Cascadia megathrust. *Pure and Applied Geophysics*, 176:3867–
485 3891, 2019.
- 486 K. Obara. Nonvolcanic deep tremor associated with subduction in southwest
487 Japan. *Science*, 296(5573):1679–1681, 2002.
- 488 R. Ohtani, J.J. McGuire, and P. Segall. Network strain filter: A new tool
489 for monitoring and detecting transient deformation signals in GPS arrays.
490 *Journal of Geophysical Research*, 115:B12418, 2010.
- 491 D.B. Percival and A.T. Walden. *Wavelet Methods for Time Series Analysis*.
492 Cambridge Series in Statistical and Probabilistic Mathematics. Cambridge
493 University Press, New York, NY, USA, 2000.
- 494 L.A. Preston, K.C. Creager, R.S. Crosson, T.M. Brocher, and A.M. Trehu.
495 Intraslab earthquakes: Dehydration of the Cascadia slab. *Science*, 302:1197–
496 1200, 2003.
- 497 G. Rogers and H. Dragert. Tremor and slip on the Cascadia subduction zone:
498 The chatter of silent slip. *Science*, 300(5627):1942–1943, 2003.
- 499 D.R. Shelly, G.C. Beroza, and S. Ide. Non-volcanic tremor and low-frequency
500 earthquake swarms. *Nature*, 446:305–307, 2007.
- 501 W. Szeliga, T.I. Melbourne, M.M. Miller, and V.M. Santillan. Southern Cas-
502 cadia episodic slow earthquakes. *Geophysical Research Letters*, 31:L16602,
503 2004.

- 504 W. Szeliga, T. Melbourne, M. Santillan, and M. Miller. GPS constraints on 34
505 slow slip events within the Cascadia subduction zone, 1997-2005. *Journal of*
506 *Geophysical Research*, 113:B04404, 2008.
- 507 A.G. Wech. Interactive tremor monitoring. *Seismological Research Letters*, 81
508 (4):664–669, 2010.
- 509 M. Wei, J.J. McGuire, and E. Richardson. A slow slip event in the south central
510 Alaska Subduction Zone. *Geophysical Research Letters*, 39:L15309, 2012.
- 511 P. Wessel and W. H. F. Smith. Free software helps map and display data. *EOS*
512 *Trans. AGU*, 72:441, 1991.

513 **Addresses**

514 Ariane Ducellier. University of Washington, Department of Earth and Space
515 Sciences, Box 351310, 4000 15th Avenue NE Seattle, WA 98195-1310.

516 Kenneth C. Creager. University of Washington, Department of Earth and
517 Space Sciences, Box 351310, 4000 15th Avenue NE Seattle, WA 98195-1310.

519 David A. Schmidt. University of Washington, Department of Earth and
520 Space Sciences, Box 351310, 4000 15th Avenue NE Seattle, WA 98195-1310.
521

⁵²² **Tables**

Table 1: Big Episodic Tremor and Slip events. The duration and the number of tremor are from the tremor catalog of [reference?](#). The event number and the magnitude are from the slow slip catalog of Michel et al. [2019].

Time	Duration (days)	Number of tremor (hours)	Event number	Magnitude
2007.06	28	398	3	6.68
2008.36	25	402	10	6.56
2009.35	24	248	16	6.49
2010.63	29	518	24	6.54
2011.60	37	479	30	6.47
2012.72	37	620	34	6.54
2013.71	27	423	41	6.58
2014.65	15	190	48	6.03
2014.89	38	385	51	6.40
2016.11	43	421	54	6.79
2017.23	19	279	59	6.61
2018.49	22	381		
2019.23	34	195		
2019.88	16	205		
2020.79	26	193		
2020.86	12	162		
2021.09	14	230		

Table 2: Magnitude 5 events from Michel et al. [2019].

Time	Event number	Magnitude	Sub-event of bigger event
2007.06	1	5.64	Yes
2007.08	2	5.91	Yes
2008.38	11	5.50	Yes
2009.16	14	5.50	No
2009.36	17	5.32	Yes
2010.63	25	5.76	Yes
2011.66	31	5.61	Yes
2011.66	32	5.32	Yes
2012.69	35	5.56	Yes
2013.74	42	5.71	Yes
2014.69	49	5.31	Yes
2014.93	52	5.39	Yes
2016.03	57	5.80	Yes
2017.13	60	5.43	Yes
2017.22	61	5.37	Yes

523 **Figure captions**

- 524 • Figure1. Details and smooth of the wavelet decomposition of a synthetics
525 signal with period 500 days and duration of the slow slip event equal to 2
526 days (left), 5 days, 10 days, and 20 days (right).
- 527 • Figure2. Bottom: Data from GPS station PGC5 without missing values
528 (black) and with missing values replaced by the sum of a straight line
529 and a Gaussian noise component (red) for two locations of the missing
530 values (left and right). Bottom to top: Corresponding ten details and
531 smooths of the wavelet composition for the original data (black) and for
532 the missing values replaced by the sum of a straight line and a Gaussian
533 noise component (red).
- 534 • Figure3. Details and smooth of the wavelet decomposition of the longitudi-
535 nal displacement recorded at GPS station PGC5.
- 536 • Figure 4. GPS stations used in this study (black triangles). The black
537 line represents the 40 km depth contour of the plate boundary model by
538 Preston et al. [2003]. The red triangles are the locations where we stack
539 the GPS data. The small grey dots are all the tremor locations from the
540 PNSN catalog.
- 541 • Figure 5. Details and smooth of the wavelet decomposition of the de-
542 trended cumulative tremor count around the third northernmost location
543 on Figure 3.
- 544 • Figure 6. Top: Stacked 8th level details of the wavelet decomposition of
545 the displacement over all the GPS stations located in a 50 km radius of a
546 given point, for the 16 locations indicated in Figure 3. Bottom: Opposite
547 of the 8th level detail of the cumulative tremor count in a 50 km radius
548 of a given point for the same 16 locations.
- 549 • Figure 7. Top: Stacked 7th level details of the wavelet decomposition of
550 the displacement over all the GPS stations located in a 50 km radius of a
551 given point, for the 16 locations indicated in Figure 3. Bottom: Opposite
552 of the 7th level detail of the cumulative tremor count in a 50 km radius
553 of a given point for the same 16 locations.
- 554 • Figure 8. Top: Stacked 6th level details of the wavelet decomposition of
555 the displacement over all the GPS stations located in a 50 km radius of a
556 given point, for the 16 locations indicated in Figure 3. Bottom: Opposite
557 of the 6th level detail of the cumulative tremor count in a 50 km radius
558 of a given point for the same 16 locations.
- 559 • Figure 9. Top: Sum of the stacked 6th, 7th and 8th level details of the
560 wavelet decomposition of the displacement over all the GPS stations lo-
561 cated in a 50 km radius of a given point, for the 16 locations indicated
562 in Figure 3. Bottom: Opposite of the sum of the 6th, 7th and 8th level

563 details of the cumulative tremor count in a 50 km radius of a given point
564 for the same 16 locations.

- 565
- 566 • Figure 10. ROC curve for the sum of the 6th, 7th, and 8th level details of
567 the wavelet decomposition. The red cross marks the true positive rate and
568 the false positive rate obtained with the thresholds used to make Figure
9.
 - 569 • Figure 11. Top: Stacked 5th level details of the wavelet decomposition of
570 the displacement over all the GPS stations located in a 50 km radius of a
571 given point, for the 16 locations indicated in Figure 3.

₅₇₂ **Figures**

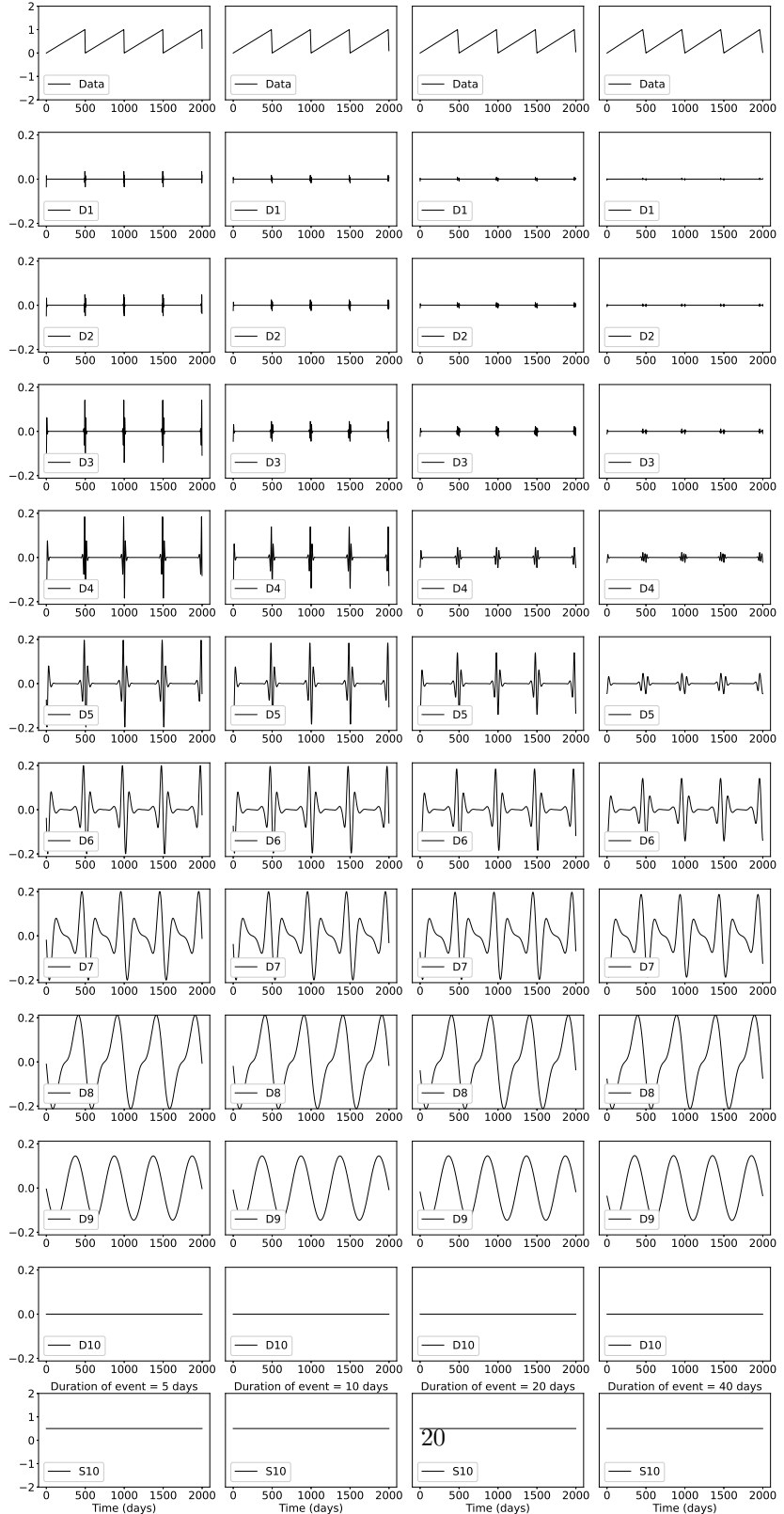


Figure 1: Details and smooth of the wavelet decomposition of a synthetics signal with period 500 days and duration of the slow slip event equal to 2 days (left), 5 days, 10 days, and 20 days (right).

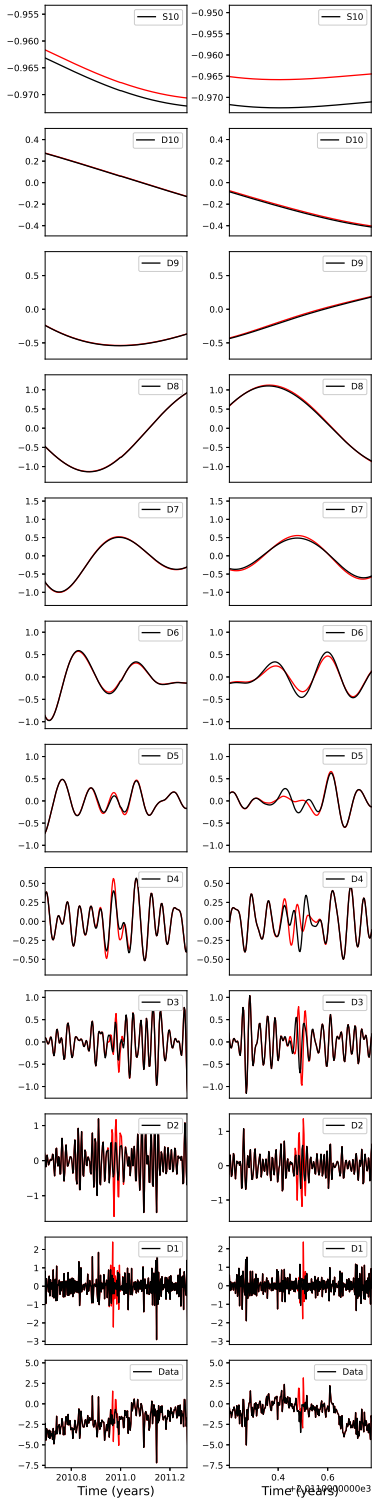


Figure 2: Bottom: Data from GPS station PGC5 without missing values (black) and with missing values replaced by the sum of a straight line and a Gaussian noise component (red) for two locations of the missing values (left and right). Bottom to top: Corresponding ten details and smooths of the wavelet composition for the original data (black) and for the missing values replaced by the sum of a straight line and a Gaussian noise component (red).

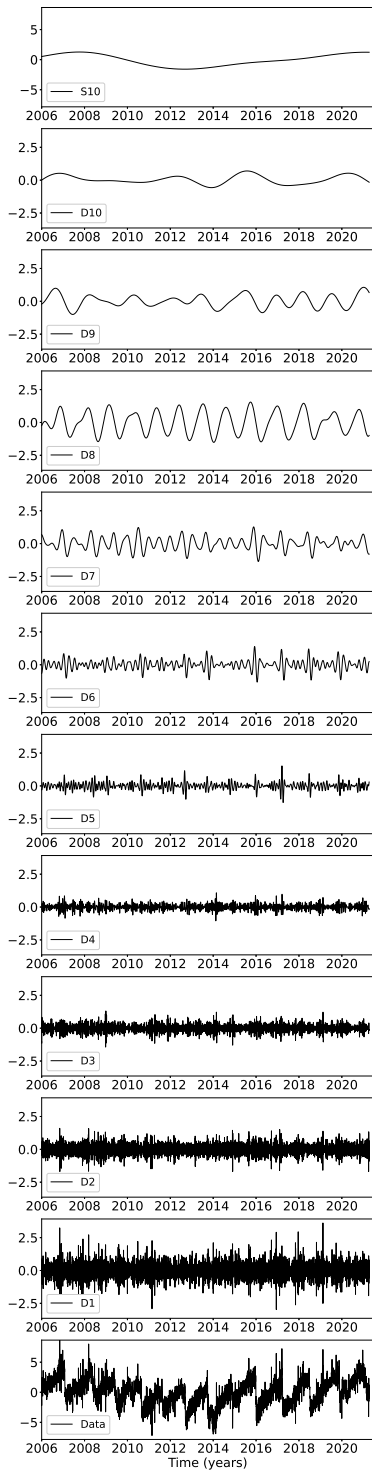


Figure 3: Details and smooth of the ²² wavelet decomposition of the longitudinal displacement recorded at GPS station PGC5.

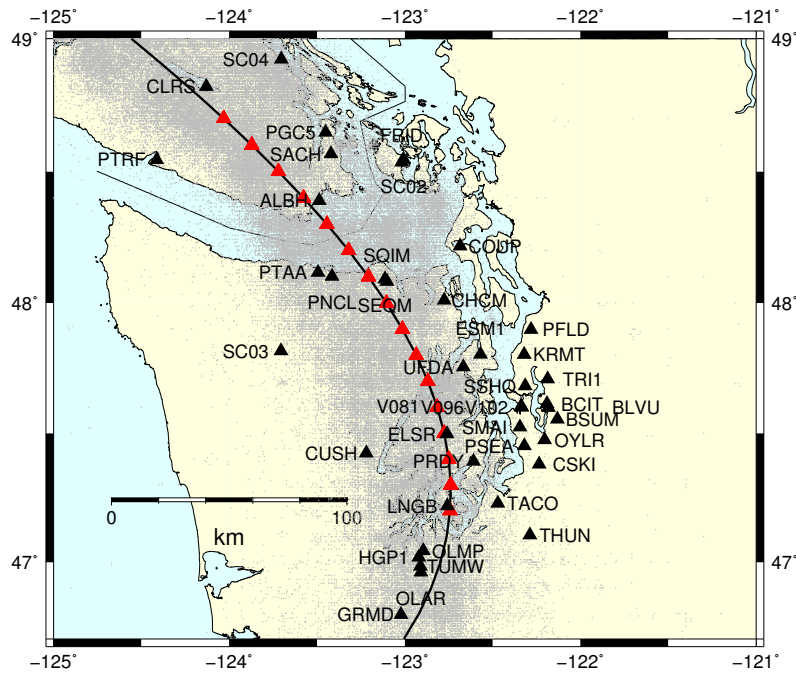


Figure 4: GPS stations used in this study (black triangles). The black line represents the 40 km depth contour of the plate boundary model by Preston et al. [2003]. The red triangles are the locations where we stack the GPS data. The small grey dots are all the tremor locations from the PNSN catalog.

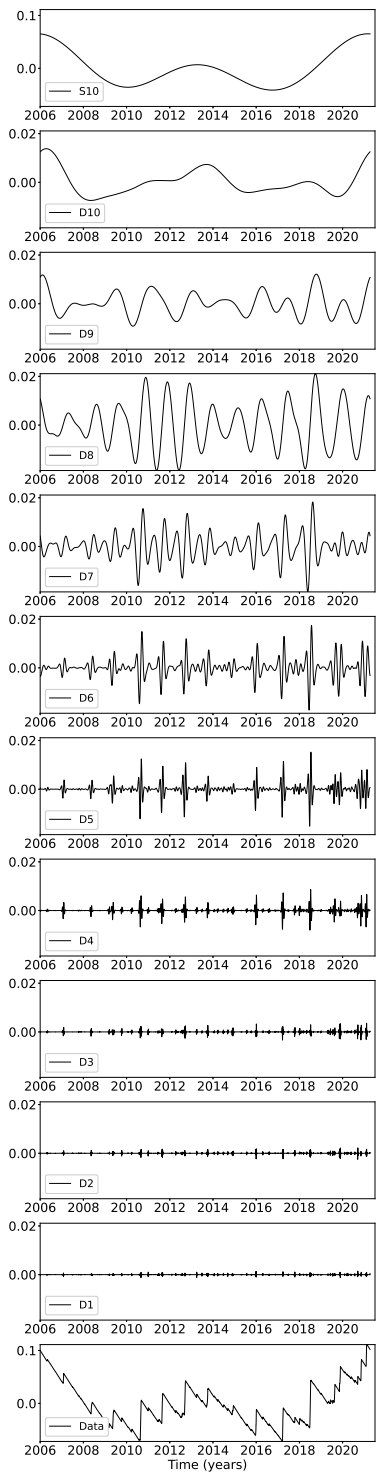


Figure 5: Details and smooth of the wavelet decomposition of the detrended cumulative tremor count around the third northernmost location on Figure 3.

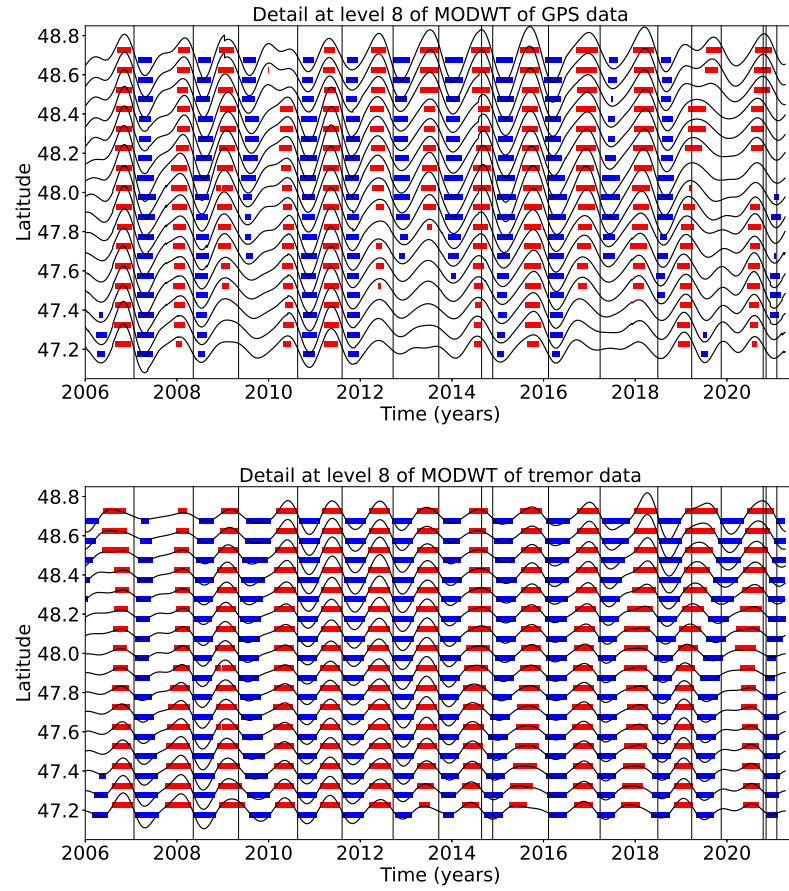


Figure 6: Top: Stacked 8th level details of the wavelet decomposition of the displacement over all the GPS stations located in a 50 km radius of a given point, for the 16 locations indicated in Figure 3. Bottom: Opposite of the 8th level detail of the cumulative tremor count in a 50 km radius of a given point for the same 16 locations.

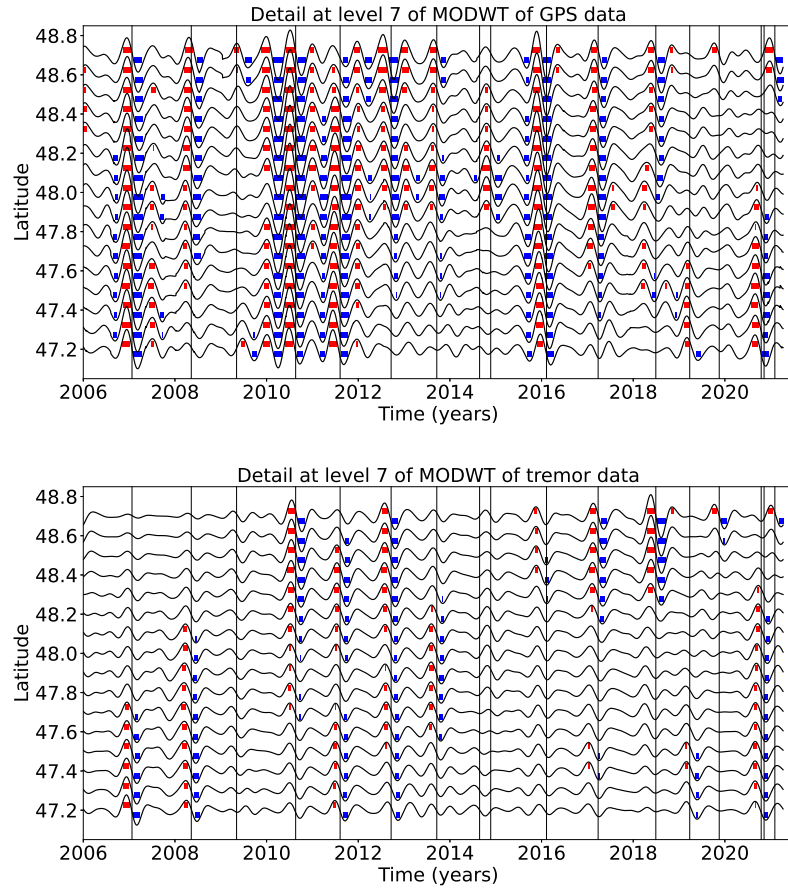


Figure 7: Top: Stacked 7th level details of the wavelet decomposition of the displacement over all the GPS stations located in a 50 km radius of a given point, for the 16 locations indicated in Figure 3. Bottom: Opposite of the 7th level detail of the cumulative tremor count in a 50 km radius of a given point for the same 16 locations.

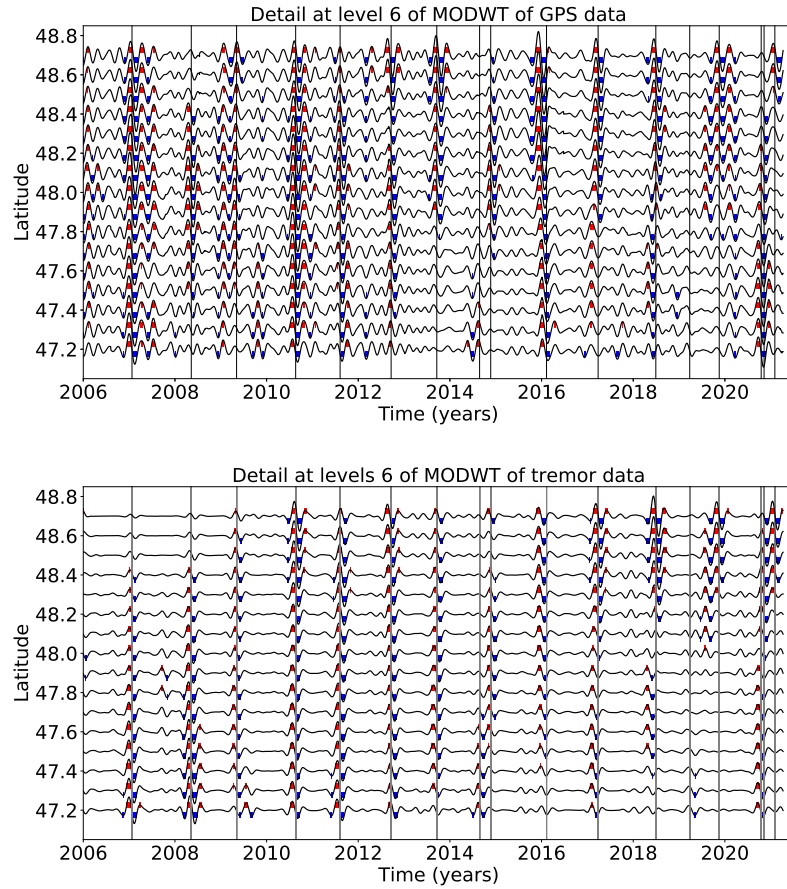


Figure 8: Top: Stacked 6th level details of the wavelet decomposition of the displacement over all the GPS stations located in a 50 km radius of a given point, for the 16 locations indicated in Figure 3. Bottom: Opposite of the 6th level detail of the cumulative tremor count in a 50 km radius of a given point for the same 16 locations.

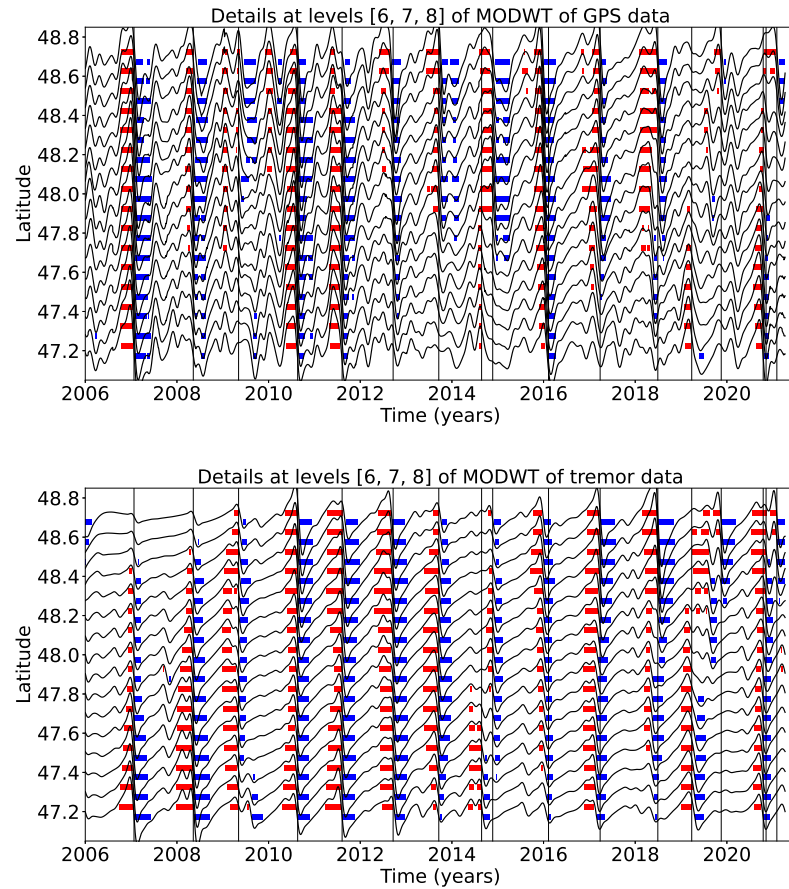


Figure 9: Top: Sum of the stacked 6th, 7th and 8th level details of the wavelet decomposition of the displacement over all the GPS stations located in a 50 km radius of a given point, for the 16 locations indicated in Figure 3. Bottom: Opposite of the sum of the 6th, 7th and 8th level details of the cumulative tremor count in a 50 km radius of a given point for the same 16 locations.

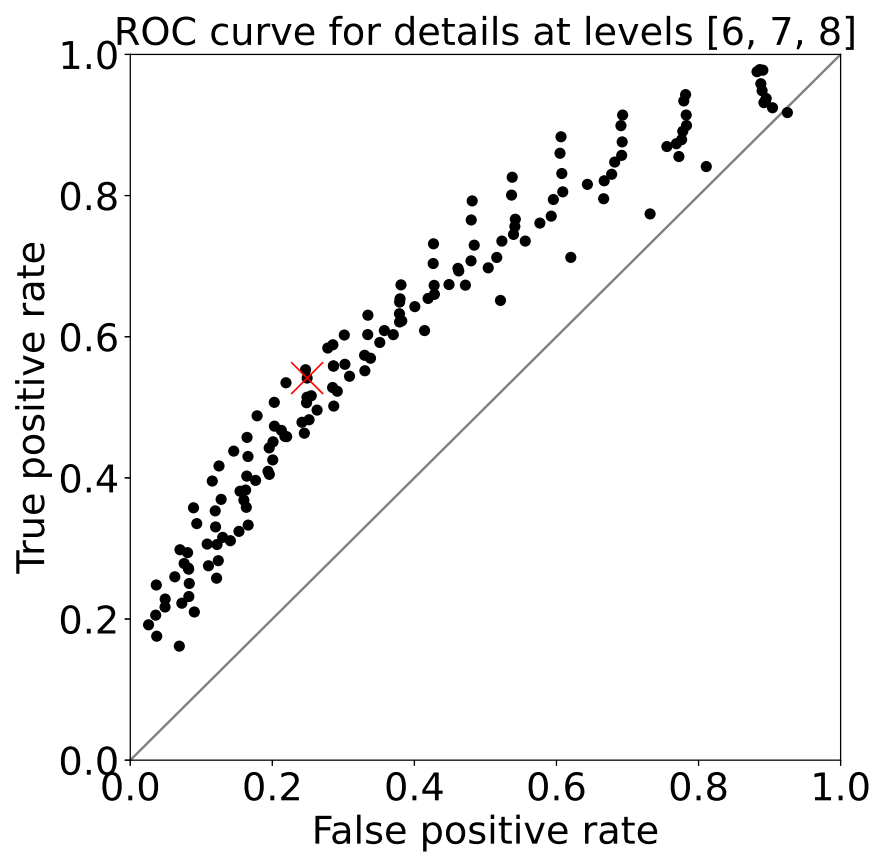


Figure 10: ROC curve for the sum of the 6th, 7th, and 8th level details of the wavelet decomposition. The red cross marks the true positive rate and the false positive rate obtained with the thresholds used to make Figure 9.

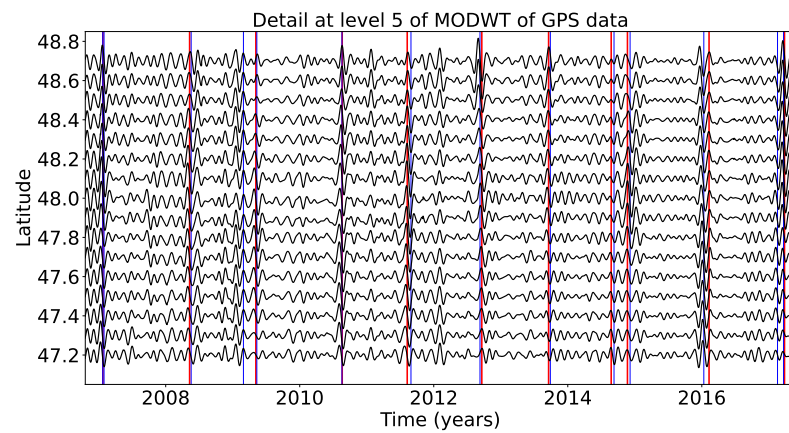


Figure 11: Top: Stacked 5th level details of the wavelet decomposition of the displacement over all the GPS stations located in a 50 km radius of a given point, for the 16 locations indicated in Figure 3.